

Application of the ASBM-SA closure in a turbulent flow over a hump in the presence of separation control.

C. F. Panagiotou^{a,b}, F. S. Stylianou^c, E. Gravanis^{e,f}, E. Akylas^{e,f}, S. C. Kassinos^{c,d}

^a *Laboratory Of Environmental Engineering (GAIA), Nireas-International Water Research Centre, University of Cyprus, Nicosia, Cyprus*

^b *Department of Civil & Environmental Engineering, University of Cyprus, Nicosia, Cyprus*

^c *Computational Sciences Laboratory (UCY-CompSci), Nireas-International Water Research Centre, University of Cyprus, Nicosia, Cyprus*

^d *Department of Mechanical & Manufacturing Engineering, University of Cyprus, Nicosia, Cyprus*

^e *Department of Civil Engineering & Geomatics, Cyprus University of Technology, Limassol, Cyprus*

^f *Eratosthenes Centre of Excellence, Cyprus University of Technology, Limassol, Cyprus*

Abstract

We demonstrate the coupling between the Algebraic Structure-Based Model (ASBM) and the one-equation SpalartAllmaras (SA) model, which provides an easy route to bringing structure information in engineering turbulence closures. The estimation ability of the hybrid model was tested for a flow over a hump model with no-flow control and steady suction. ASBM-SA model produced satisfactory predictions for the streamwise Reynolds stress component, while a qualitative agreement with the experiments was achieved for the transverse component. Regarding the shear stress component, ASBM-SA closure provides improved predictions compared to SA in the entire domain.

1 Introduction

The class of RANS models most often used in engineering applications is that of Eddy Viscosity Models (EVM). One of the most popular EVM is the SpalartAllmaras (SA) one-equation model [1]. The SA model is often favored by practicing engineers because it exhibits superior robustness, low CPU time requirements and substantially lower sensitivity to grid resolution compared to two-equation models. On the other hand, one has to recognize that, despite its computational and implementational attractiveness, the eddy viscosity assumption is also the source of some of the most important performance limitations. For example, like other EVM, the SA model fails to capture important flow features, such as turbulence anisotropy or the effects of mean or system rotation. A common feature of the classical closure approaches described so far is the assumption that all key information about the turbulence is contained in the scales of the turbulence and in the turbulence stress tensor. However, one should consider that the turbulent stresses contain information only about the componentality of the turbulence, i.e. about the directions in which the turbulence fluctuations associated with large-scale eddies are most energetic. Thus, traditional closures do not take into account the morphology of the energy-containing eddies. Yet, eddies tend to organize spatially

the fluctuating motion in their vicinity. In doing so, they eliminate gradients of fluctuation fields in some directions (those in which the spatial extent of the structure is significant) and enhance gradients in other directions (those in which the extent of the structure is small). Thus, associated with each eddy are local axes of dependence and independence that determine the dimensionality of the local turbulence structure. This structure dimensionality information is complementary to the componentality information contained in the Reynolds stresses, and as Kassinos & Reynolds [2] and Kassinos et al. [3] have shown, it is dynamically important. A detailed description of the complete set of the turbulence structure tensors is given in several works [3, 4, 5].

The significant effect that the morphology of the large-scale structures has on the evolution of turbulent statistics [6] has motivated the development of structure-based models. These models can be classified into two categories: differential and algebraic. The first category involves solving a set of transport equations to evaluate structure tensors. Simplified models have been proposed that are applicable at the homogeneous limit [7, 8, 9], while a more sophisticated differential model was proposed by Poroseva et al. [10] that was tested in a turbulent flow passing through a cylindrical pipe that rotates around its longitudinal axis. Furthermore, structure-based models were recently constructed to evaluate scalar transport, ranging from simple passive scalars [5, 11] to strongly stably stratified flows [12].

The second category refers to algebraic approaches, which are based on assumptions that lead to constitutive equations. The Algebraic Structure-Based Model (ASBM) [13, 14] is an engineering structure-based turbulence model that follows this second approach. It is a fully realizable two-equation structure-aware model that provides the full Reynolds stress tensor. Panagiotou & Kassinos [15] presented a successful coupling between the ASBM with the one-equation SA model. Their intention was to combine the numerical robustness and stability of the SA model along with the deeper physical content of the ASBM. The performance of the hybrid model, called ASBM-SA, was evaluated in several standard benchmark cases, ranging from simple fully-developed channel flows to a flow over a steep hill, achieving an overall good agreement between model and experimental predictions. Hence, the aim of this study is to evaluate the performance of the ASBM-SA closure to a more complex case, in particular the case of turbulent flow over a two-dimensional hill with and without separation control.

2 Coupling between ASBM and the SA model

The main limitation of SA (and any other one-equation model) is that it does not provide of a complete set of turbulence scales. On the other hand, the ASBM closure relies on the availability of suitable turbulence scales and this was the key stumbling block in trying to couple the ASBM and SA closures. The Bradshaw hypothesis [16] has been used as the starting point for transforming turbulence scales $\kappa - \epsilon$ closures, where κ and ϵ are the turbulent kinetic energy and energy dissipation rate respectively, to one equation models. Here, our objective is to use the same phenomenology in order to extract these scales from the SA one-equation

closure. A complete description of this formulation and on how the coupling between the two closures has been achieved can be found in Panagiotou & Kassinos [15].

3 Results and discussion

3.1 Outline

In this study we have considered the case of no-flow control, as well as the case where active-control is applied via steady-suction. During the CFDVAL2004 Workshop [17], these two cases were investigated in depth to assess the performance of popular engineering turbulence models in strongly separated flows subjected to favorable/adverse pressure gradients. Experiments have been conducted in the NASA Langley Transonic Cryogenic Tunnel by Greenblatt et al. [18]. The shape of the hump is that of a “Modified Glauert-Goldschmied” hill, similar to the one used by Seifert and Pack [19]. The experiments are nominally two-dimensional (2D), despite the presence of three dimensional (3D) effects near the side end-plates. The scenarios involved both uncontrolled and controlled flow (steady suction) for Reynolds numbers (Re) ranging from 0.37 up to 1.1 million, corresponding to Mach numbers (M) ranging from 0.04 up to 0.12. One no-flow control case and one active-control case were selected for the extraction of detailed experimental measurements. Figure 1 shows the geometry of the whole domain, including a detailed view of the flow control slot. The chord length of the hump is denoted as c , the height of the domain H is 90% the chord length, while the maximum height of the hump is approximately $0.13 c$. The slot is located near $x/c \approx 0.65$, where the slot width h is $0.00187 c$. Detailed information regarding the geometry, computational grids and the relevant experiments can be found in [20]. One of the conclusions reached during the CFDVAL2004 Workshop is that blockage effects stemming from the presence of side plates need to be accounted for in simulations, otherwise the computed pressure coefficients levels exhibit significant discrepancy relative to the experiments, especially over the hump. Thus, the top tunnel surface around hump location is modified so as to reflect the change in the tunnel cross-sectional area due to the presence of the side-plates, as described in [20].

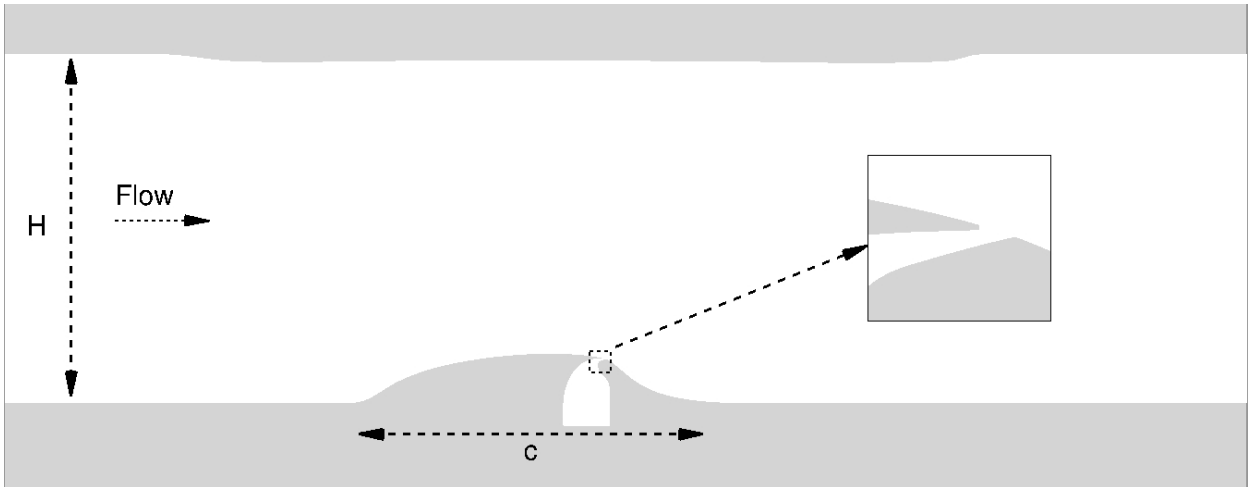


Figure 1: Sketch of the geometry, with a modification along the top-surface such as to account for the side-plate effects, as described in [20].

3.2 Validation cases

3.2.1 Turbulent boundary layer

As a first step, we performed steady computations of a spatially developing boundary layer flow over a flat plate for flow conditions that correspond to the experiments of Greenblatt et al. [18]. Profiles of the converged solution at a specific streamwise location were extracted and then used as inlet boundary conditions for the cases involving the 2D hump. The desired Reynolds number is $Re_\delta \approx 68200$ based on the freestream velocity U_∞ , where subscript ∞ denotes freestream values, and the boundary layer thickness $\delta \approx 0.074c$. At the inlet, Dirichlet boundary conditions are imposed for the mean streamwise velocity U_x and the pseudo-viscosity $\tilde{\nu}$ variables, such as $\tilde{\nu}_\infty/\nu \approx 3$ and $U_\infty = 0.1 M$, yielding a freestream Reynolds number $Re_\infty = 929,000$ based on the chord length c of the hump, air viscosity ν and the freestream velocity U_∞ . At the outlet, a penalty condition is imposed to prevent the occurrence of reflectional effects while ensuring mass conservation. A slip condition was imposed at the top surface, a no-slip condition at the bottom wall surface and periodic conditions along the spanwise direction. In order to obtain grid-independent solutions, three different meshes of increasing resolution were considered. For each mesh, geometric functions were used to define the normal distribution of the nodes, while uniform spacing has been adopted along the streamwise direction. Grid 1 contains a non-uniform mesh of size $120 \times 90 \times 1$ along the streamwise, wall-normal and spanwise directions respectively. The corresponding size for Grid 2 is $130 \times 120 \times 1$ and for Grid 3 is $140 \times 150 \times 1$. The finest grid yields a value of y^+ around 0.5 for the wall-adjacent cell at the location of the extracted data. Figures 2a-b show predictions using the SA closure for the streamwise mean velocity and pseudo-viscosity respectively. In Figure 3 we show a comparison between the predictions of the SA model using Grid 3 as the baseline grid, and the experimental data for the streamwise mean velocity U_x , yielding a good agreement.

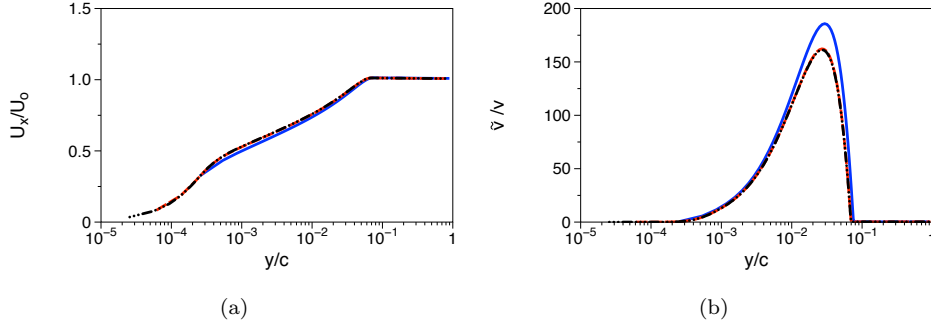


Figure 2: Grid-convergence analysis for a spatially developing turbulent boundary layer at $Re_\delta \approx 68,200$. SA model predictions for (a) the streamwise mean velocity and (b) the pseudo-viscosity. Comparison is made among three different grids: Grid 1 (—); Grid 2 (----); Grid 3 (-·-·-).

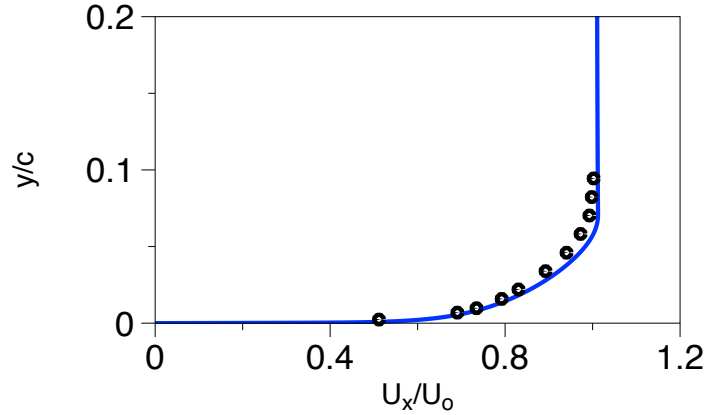


Figure 3: SA model predictions (lines) for the streamwise mean velocity. Comparison is made to the experiments (symbols) of Greenblatt et al. [18].

3.2.2 No-flow control

The case of flow over a hump having the shape of “Modified Glauert” hill is considered next. This case was originally conceived for testing the ability of active control to reduce the size of the existing recirculation bubble. However, from a turbulence modeling perspective, even the uncontrolled case is interesting due to the presence of strong separation, which proves to be challenging to turbulence engineering models. Thus, in our numerical experiments, we considered first the uncontrolled case of flow. Simulations have been performed using SA and ASBM-SA models, which are compared to the experimental work of Greenblatt et al. [18] At the inlet surface, profiles for the variables are obtained from the SA solution for the turbulent boundary layer corresponding to $Re_\delta \approx 68200$ as described in the previous subsection. At the floor surface, as well as at the wall surfaces inside the cavity, solid wall (no-slip) boundary conditions were applied. A penalty condition is imposed at the outlet surface to ensure that mass flow exits the domain properly, while slip conditions are used at the top surface and periodic conditions for the spanwise direction. Two grids

were considered to conduct a grid-sensitivity analysis. The coarser grid contains approximately 103,000 grid points, whereas the finer grid possesses approximately 160,000 grid points. Mesh details are shown in Figure 4, together with a zoomed view of the cavity region.

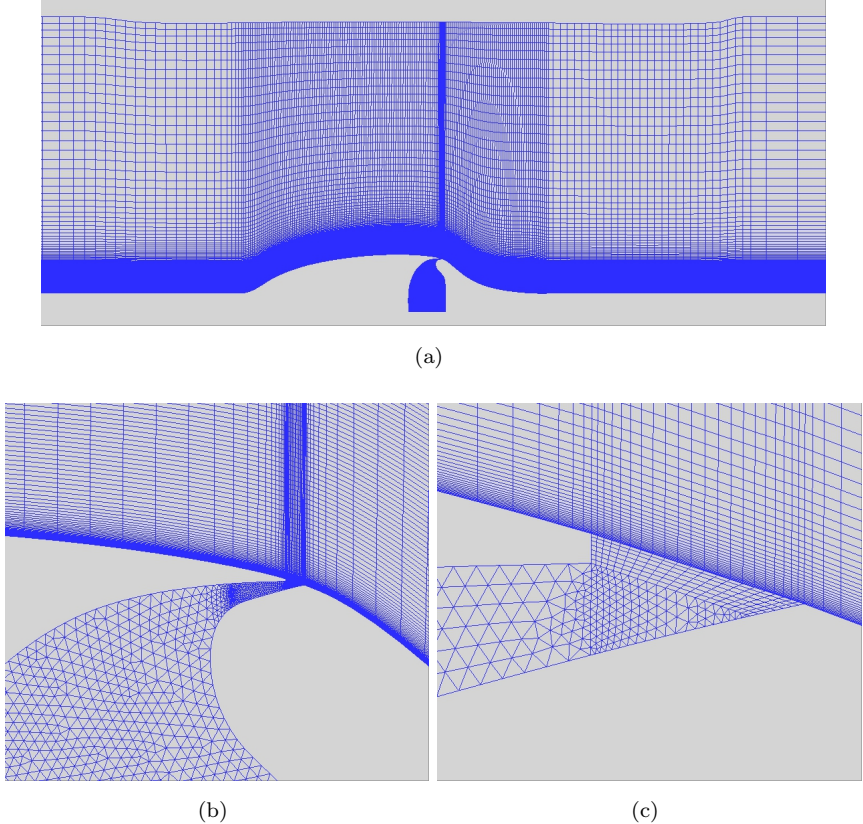


Figure 4: Unstructured computational grid with details of the slot region.

Figures 5a-b show SA model predictions for the wall-static pressure coefficient $c_p = (p - p_0)/\frac{1}{2}\rho U_\infty^2$ and skin-friction coefficient $c_f = \tau_w/\frac{1}{2}\rho U_\infty^2$ respectively. Based on these results, the coarser grid is shown to be fine enough for the current case.

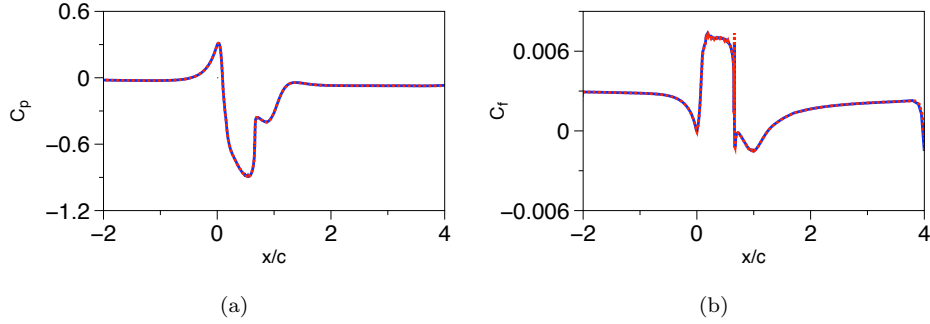


Figure 5: Effect of grid on SA model predictions for the uncontrolled case, for (a) the wall-static pressure coefficient and (b) the skin-friction coefficient. Two grids are shown: coarse grid (—); fine grid (---).

Due to the algebraic nature of the ASBM closure, numerical difficulties are encountered for the cases where strongly separated flows are considered, as the present ones. During previous works, a filtering scheme was applied in order to smoothen the profiles, improving that way the numerical stability of the solution. However, use of this scheme in the current case led to a mismatch between SA and ASBM-SA predictions for the skin-friction coefficients in regions where a good agreement was expected, such as upstream of the leading edge of the hill and downstream of the recirculation region. As a result, we separated the domain into two zones, one prior the leading edge where the filtering scheme is not active, and the region downstream the leading edge where the scheme is switched on (Figure 6). Figure 7 shows a comparison between SA and ASBM-SA predictions using both approaches for the filtering scheme, revealing the significant role that the filtering details play on the skin-friction distribution all along the bottom surface. In contrast, the pressure coefficient remains unaffected by the choice of filtering scheme.

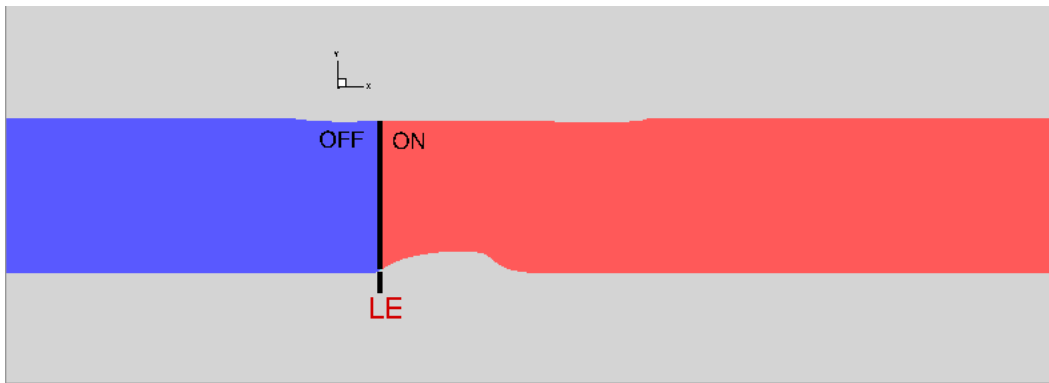


Figure 6: Separation zones showing where the filtering scheme is active (on) or not (off).

Figure 8 displays the evolution of the maximum mean streamwise velocity residual. The residual is divided by its initial value, denoted by subscript 0, and is defined by

$$\text{Residual} = \max \left[\frac{V \times \Delta U_x / \Delta t}{(V \times \Delta U_x \Delta t)_0} \right], \quad \Delta U_x = U_x^{n+1} - U_x^n, \quad (1)$$

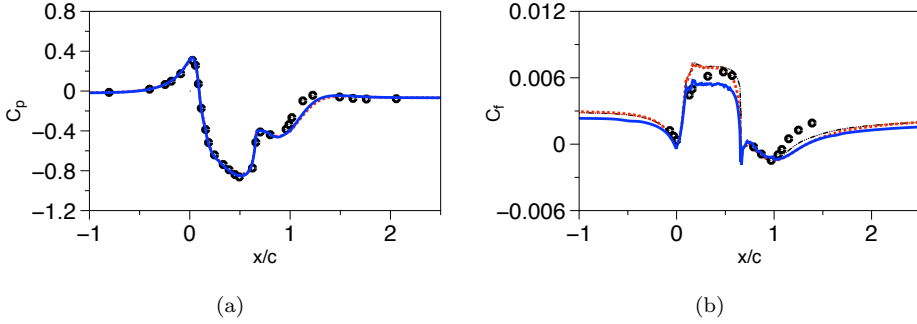


Figure 7: Effect of zonal filtering on (a) the wall static-pressure coefficient and (b) the wall skin-friction coefficient for the no-flow control case. SA (----) and ASBM-SA (-·-·-) are compared to the ASBM-SA predictions when filtering is active in the entire domain (—) and the experimental values (symbols) of Greenblatt et al. [18].

where n refers to the n -th iteration, Δt to the time step and V to the volume of the corresponding cell. For both SA and ASBM-SA models, a drop of at least 5 orders of magnitude for the residuals compared to the initial field is achieved, which is believed to be sufficient to provide time-converged solutions.

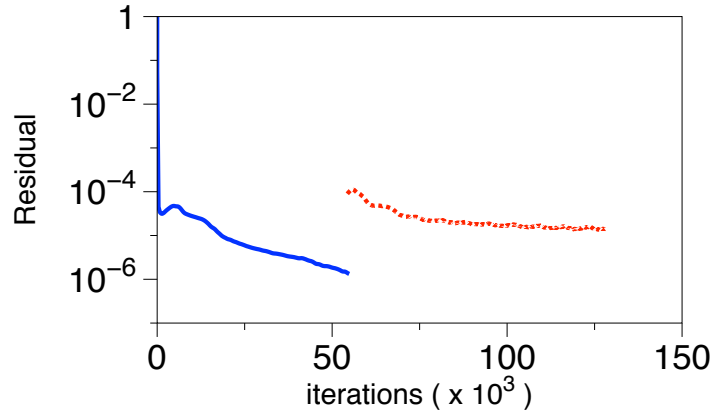


Figure 8: Time history of the streamwise mean velocity residual for the uncontrolled case. The sudden jump in the residual levels indicates the point where the ASBM coupling is switched on.

In order to both accelerate our simulations and overcome some stability issues related to the ASBM-SA computations inside the cavity in the case of no-suction, additional computations using similar meshes but without the presence of the cavity were conducted. For these cases, we considered a solid-wall condition along the slot exit. Figures 9a-b show SA predictions for the mean velocity streamlines at the vicinity of the hump in the presence and absence of the cavity respectively, demonstrating the trivial discrepancies between the two approaches. Figure 10 shows the corresponding comparison for the wall-static pressure coefficient, which again reveals the negligible effect on the results of the cavity absence when the flow control is inactive (no suction).

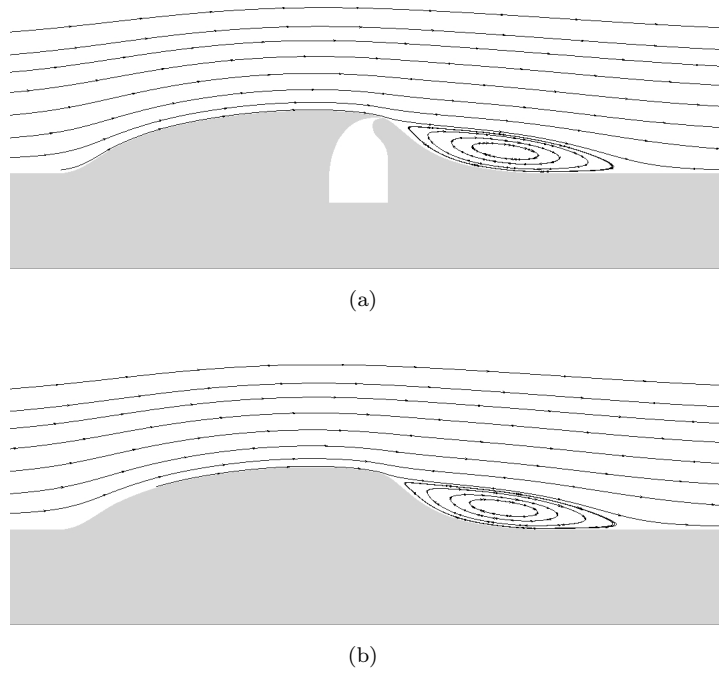


Figure 9: SA model predictions for the streamlines of the mean flow approaching the hump (a) in the presence of the cavity and (b) in the absence of the cavity.

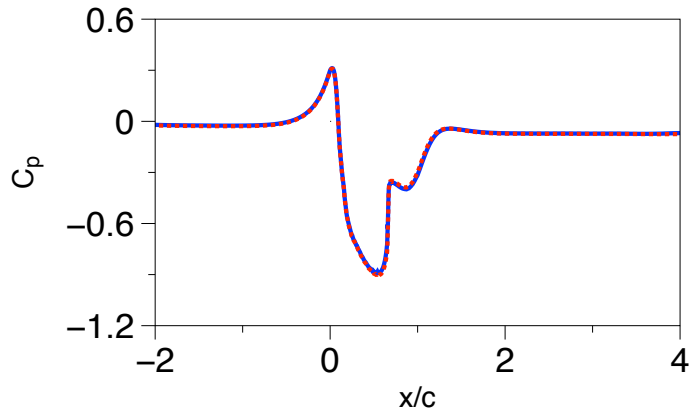


Figure 10: SA model predictions in the presence (—) or absence (----) of the cavity for the wall-static pressure coefficient.

In the following figures, all turbulent and mean quantities (except c_f , c_p) are normalized based on the chord length c and the reference inlet freestream velocity U_∞ . Setting the leading edge of the hump as the origin of the streamwise distance ($x/c = 0$), profiles are extracted at three different stations inside the recirculation bubble as measured by the experiments ($x/c = 0.66, 0.8, 1.0$) and one station at the recovery region ($x/c = 1.2$), denoted as stations A, B, C, D respectively (Figure 11).

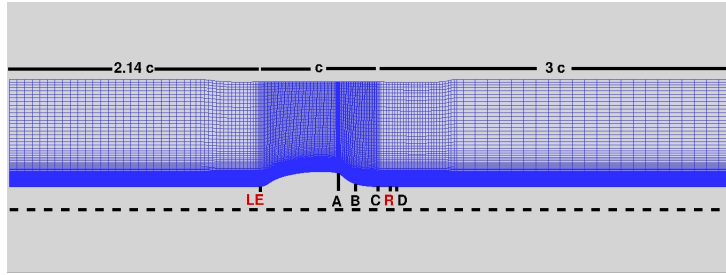


Figure 11: Geometrical and mesh details in the absence of cavity. Data is extracted at four stations, denoted as A, B, C and D. The leading-edge point (LE) and the re-attachment point (R) are also shown.

Figure 12 shows the predictions of the ASBM-SA and SA closures for the variation of the pressure (c_p) and skin friction (c_f) coefficients along the wall surface. Comparison is made to experimental measurements. The ASBM-SA model captures accurately the peak magnitude of the pressure coefficient around $x/c \approx 0.57$. For x/c ranging from -1 to 1.1, that is from the inlet up to about the re-attachment point, the ASBM-SA provides slightly improved c_p predictions when compared to SA. Right after re-attachment though, the ASBM-SA predicts a slightly delayed recovery of c_p as compared to the experiments (and the SA closure). The two models produce comparable agreement with the experiments for the skin-friction coefficient. ASBM-SA provides an improvement right after the upstream edge of the hill ($x/c \approx 0.2$), while SA predicts correctly the magnitude near the sharp geometry change that occurs around $x/c \approx 0.65$. According to Table 1, both models overpredict the recirculation bubble, with ASBM having the tendency to delay the re-attachment of the flow further downstream, an observation which is in agreement with previous cases in which separated flows over 2D hills were considered, such as the “Witch of Agnesi” hump, as described in detail in [15]. Figure 13 shows results for the streamwise mean velocity U_x at the four stations. As shown in Figures 13a-b, at the first two stations ASBM-SA provides slightly improved predictions relative to the SA model, while SA is in better agreement with the experimental data at the next two stations, mostly due to the greater delay of re-attachment in the ASBM-SA predictions.

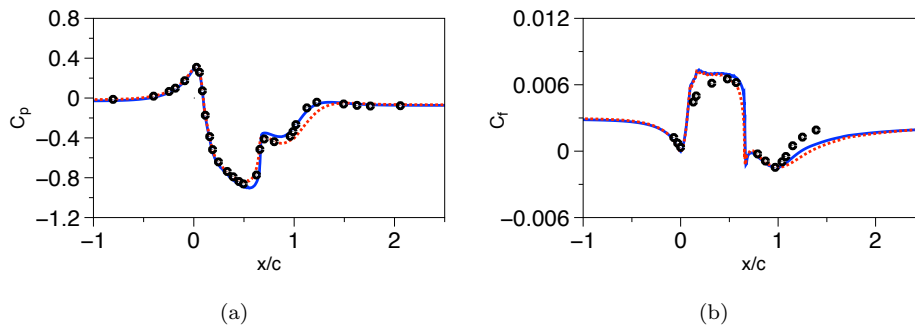


Figure 12: SA (—) and ASBM-SA (----) model predictions for the no-flow control case for (a) the wall static-pressure coefficient and (b) the wall skin-friction coefficient. Comparison is made to experimental values (symbols) of Greenblatt et al. [18].

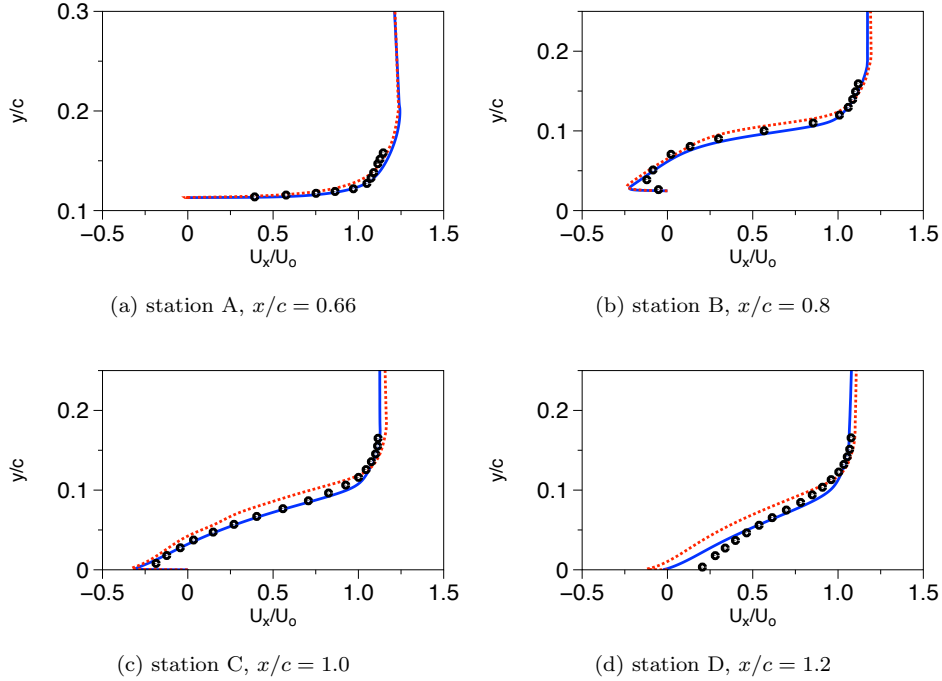


Figure 13: Turbulent flow over the “Glauert-Goldschmied” 2D hill for the no-flow control case. Model predictions for the streamwise mean velocity U_x at various x -stations for SA (—) and ASBM-SA (---) closures. Comparison is made to experimental values of Greenblatt et al. [18].

Next, we consider the performance of the ASBM-SA closure for the turbulent intensities and the fluctuating shear stress with respect to experimental results. The SA model is included only in the comparison for the fluctuating shear stress component, since it cannot provide predictions for the turbulent intensities. Figure 14 displays the streamwise Reynolds stress component R_{xx} . At station A, ASBM-SA yields reasonable predictions, being able to capture the near-wall peak magnitude. At the remaining three stations ($x/c = 0.8, 1.0, 1.2$), ASBM-SA is able to capture satisfactorily the peak magnitude. We note that the wiggles near $y/c = 0.2$ at station A (Figure 14a) originate from the algebraic expressions for the estimation of the turbulent kinetic energy (not shown here). Following term by term the algebraic procedure for the calculation of kinetic energy, we found that this issue is most likely related to the local mean velocity gradients. These wiggles are also present in previous works [15], for which similar findings were deduced. We also point out that the location $y/c = 0.2$ at which the wiggles appear is close to the interface between two grid blocks. Overall, we believe that this is a localized effect that does not affect the quality of the solution.

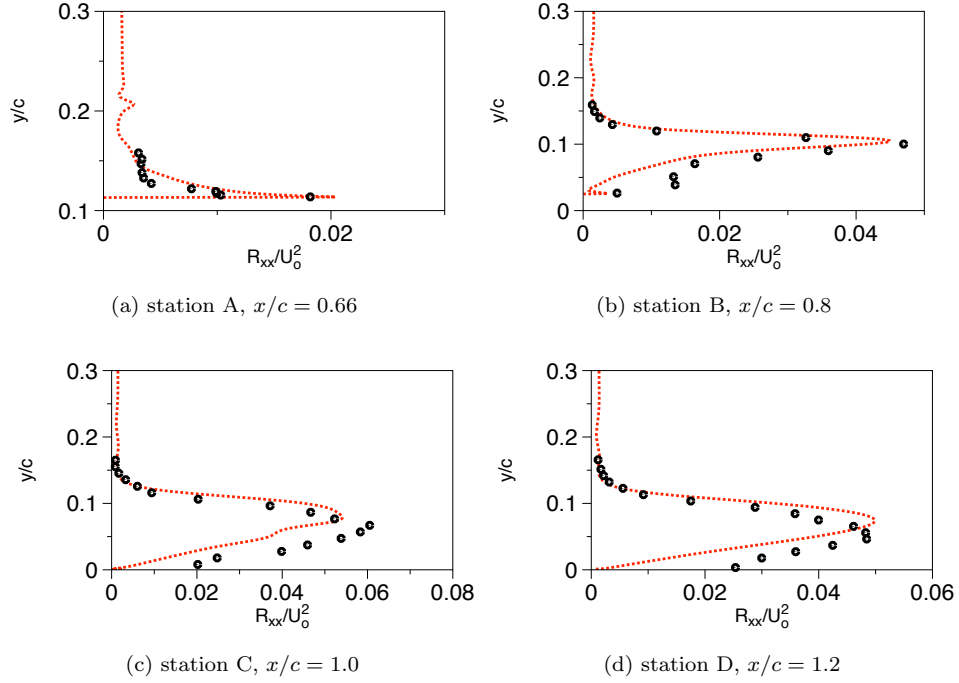


Figure 14: Turbulent flow over the “Glauert-Goldschmied” 2D hill for the no-flow control case. ASBM-SA model predictions (lines) for the streamwise Reynolds stress component R_{xx} at various x -stations are shown. Comparison is made to experimental values (symbols) of Greenblatt et al. [18].

Figure 15 depicts the corresponding predictions for the transverse Reynolds stress component R_{yy} . ASBM-SA closure strongly overpredicts the near-wall magnitude at station A, while a fair agreement with the experiments is achieved at the remaining stations.

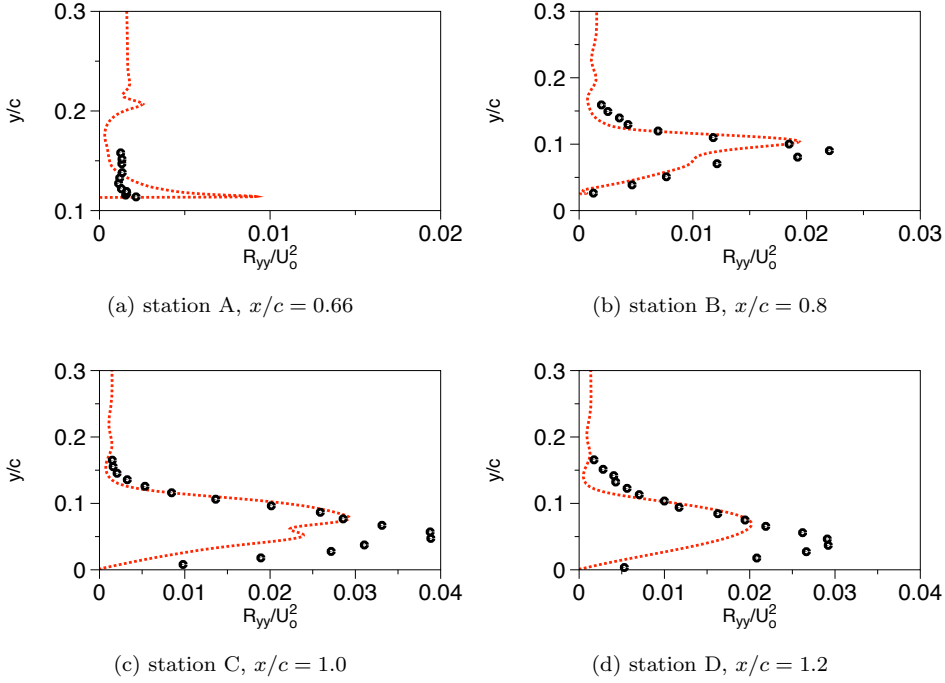


Figure 15: Turbulent flow over the “Glauert-Goldschmied” 2D hill for the no-flow control case. ASBM-SA model predictions (lines) for the transverse Reynolds stress component R_{yy} at various x -stations are shown. Comparison is made to experimental values (symbols) of Greenblatt et al. [18].

Figure 16 shows SA and ASBM-SA predictions for the fluctuating shear stress component. At the first station, ASBM-SA exhibits a similar behavior as for the transverse Reynolds stress component. At the remaining three stations, ASBM-SA provides noticeable improvement relative to the SA model, in both the near-wall and freestream regions. This improvement is evident in the whole range of the recirculation bubble, suggesting a satisfactory response of the hybrid model to the strong anisotropic effects that characterize this region.

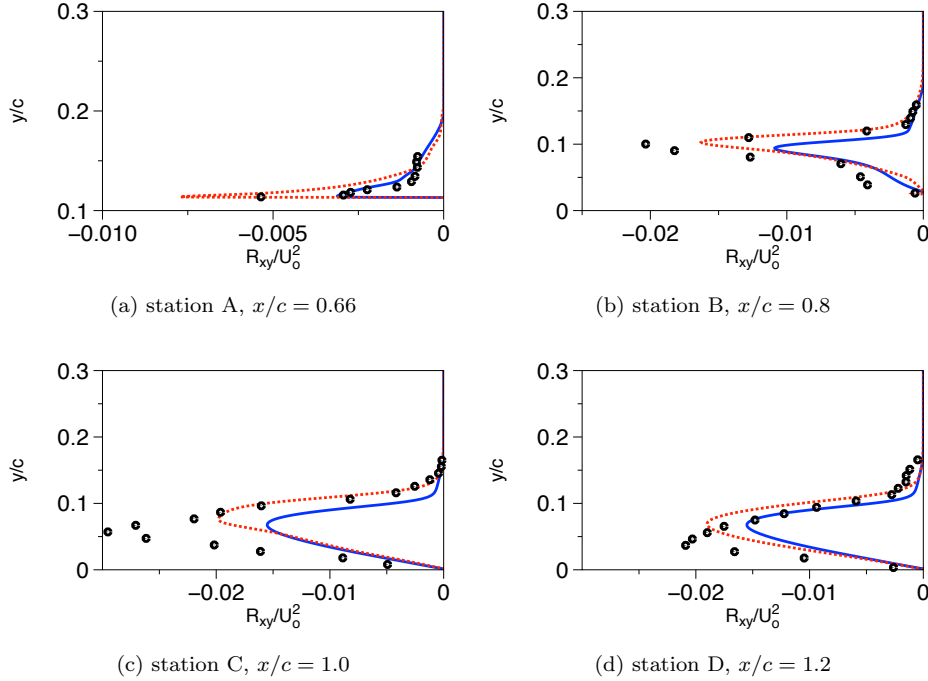


Figure 16: Turbulent flow over the “Glauert-Goldschmied” hill for the no-flow control case. Model predictions for the shear stress component R_{xy} at various x -stations for SA and ASBM-SA closures. Comparison is made to experimental values of Greenblatt et al. [18].

3.2.3 Control via steady suction

As a first step, we define the steady mass transfer momentum coefficient

$$c_\mu = \frac{\rho h U_{jet}^2}{1/2 c \rho U_o^2}, \quad (2)$$

where U_{jet} denotes the jet velocity. For the current case, c_μ is set equal to 0.241%, corresponding to a constant mass flow rate of $\dot{m} = 0.01518 \text{ kg/s}$ being sucked through the slot, in order to match the experimental conditions of Greenblatt et al. [18]. Figure 17 shows ASBM-SA model predictions for the wall-normal spacing along the floor surface for the uncontrolled and controlled cases, needed to ensure that our solutions are obtained in sufficiently resolved grids. As expected, a sharp increase in y^+ levels occurs at the location of the slot exit where no-wall is present.

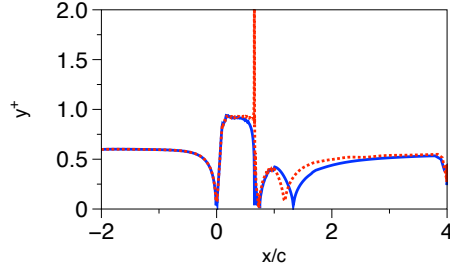
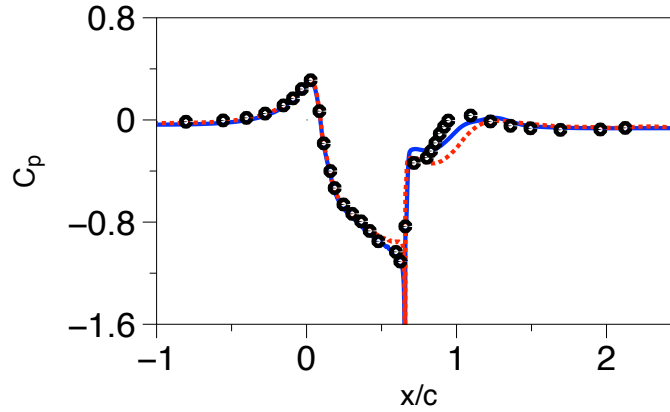


Figure 17: ASBM-SA model predictions for the streamwise variation at the bottom surface for the normal spacing at the wall normalized in wall-units. Results are shown for both the no-flow control (—) and the steady-suction (----) cases.

Results for the wall-static pressure coefficient are shown in Figure 18, where the predictions of the SA and ASBM-SA models are compared to the experimental data of Greenblatt et al. [18]. The ASBM-SA closure manages to capture accurately the magnitude and the location of the first sharp change right after the slot, located around $x/c \approx 0.67$, followed by a small recovery delay, as compared to the SA model, till the trailing edge of the hill ($x/c = 1$) where the two models coincide again.



(a)

Figure 18: SA (—) and ASBM-SA (----) model predictions for the steady-suction case for the wall static-pressure coefficient. Comparison is made to experimental values of Greenblatt et al. [18].

Figure 19 displays results for the streamwise mean velocity U_x at the four stations. As shown, SA provides slightly better agreement with the experiments than the ASBM-SA model. Figure 20 shows the corresponding comparison for the transverse mean velocity U_y . In general, SA predictions are in better agreement with the experimental data compared to ASBM-SA model.

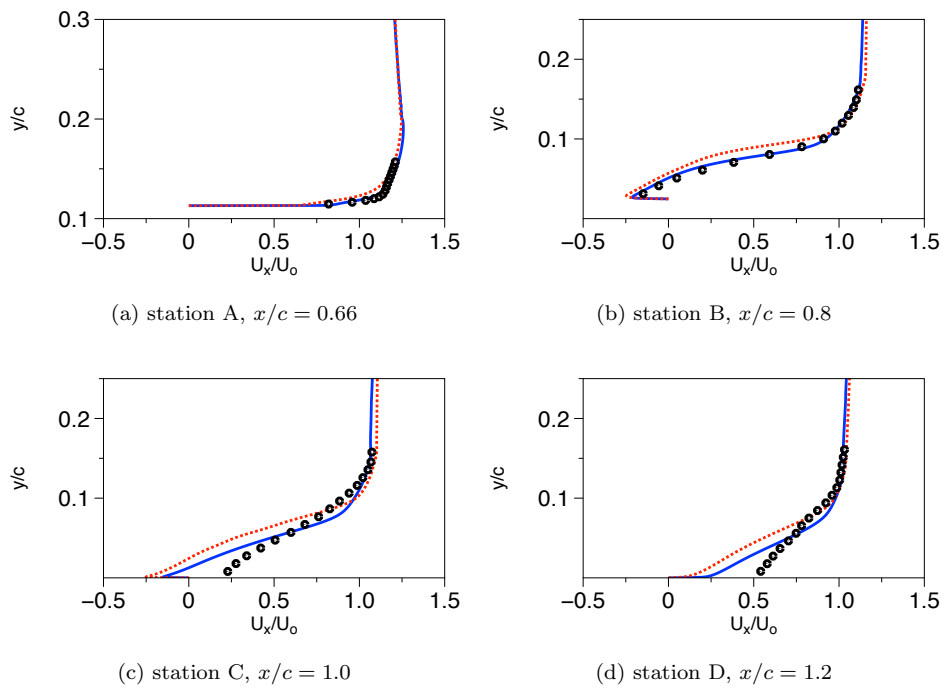


Figure 19: Turbulent flow over the “Glauert-Goldschmied” hill for the steady-suction case. Model predictions for the streamwise mean velocity U_x at various x -stations for SA and ASBM-SA closures. Comparison is made to experimental values of Greenblatt et al. [18].

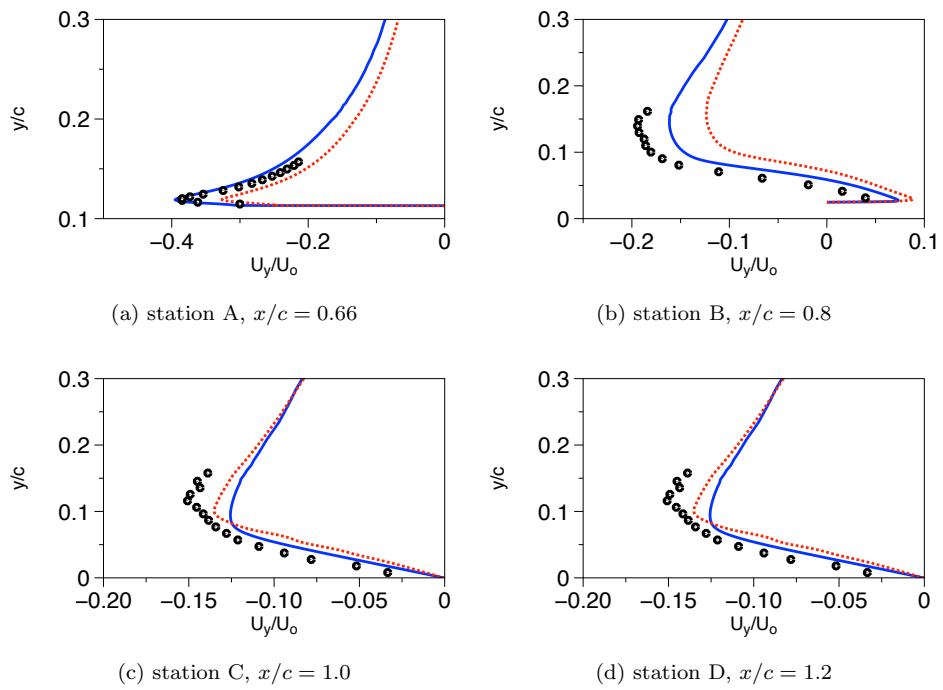


Figure 20: Turbulent flow over the “Glauert-Goldschmied” hill for the steady-suction case. Model predictions for the transverse mean velocity U_y at various x -stations for SA and ASBM-SA closures. Comparison is made to experimental values of Greenblatt et al. [18].

Table 1 shows details regarding the recirculation region. SA predicts more accurately the re-attachment point for both cases, providing an indication why SA closure obtains better results than the hybrid model for the mean statistics.

Case	Model	sep.loc.	sep.loc.	Error (%)	reatt.loc.	reatt.loc.	Error (%)
		experiment	CFD		experiment	CFD	
no-flow control	SA	≈ 0.67	0.663	1.0	1.11 ± 0.003	1.235	11.3
no-flow control	ASBM-SA	≈ 0.67	0.656	2.1	1.11 ± 0.003	1.330	19.8
steady suction	SA	≈ 0.68	0.676	0.6	0.94 ± 0.005	1.113	18.4
steady suction	ASBM-SA	≈ 0.68	0.665	2.2	0.94 ± 0.005	1.180	25.5

Table 1: Details of SA and ASBM-SA model predictions regarding the recirculation bubble for each case. Comparison is made to the experimental work of Greenblatt et al [18].

Figure 21 shows the corresponding comparison for the streamwise Reynolds stress component R_{xx} . At three of the four stations, ASBM-SA correctly predicts the near-wall peak magnitude and the freestream values, yielding a fair agreement with the experiments.

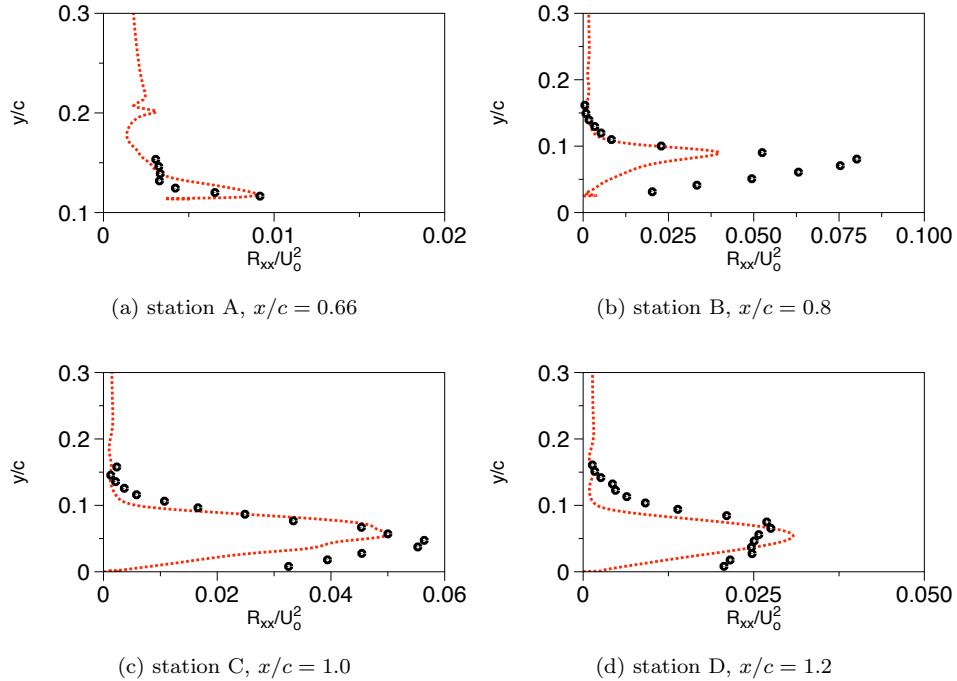


Figure 21: Turbulent flow over the “Glauert-Goldschmied” hill for the steady-suction case. Model predictions for the streamwise Reynolds stress component R_{xx} at various x -stations for SA and ASBM-SA closures. Comparison is made to experimental values of Greenblatt et al. [18].

In Figure 22, the agreement is qualitative between the ASBM-SA predictions and the experimental

measurements for the transverse Reynolds stress component R_{yy} . Combining these results with the analogous ones for R_{xx} reveals the sensitivity of the algebraic model to the anisotropic nature of the flow.

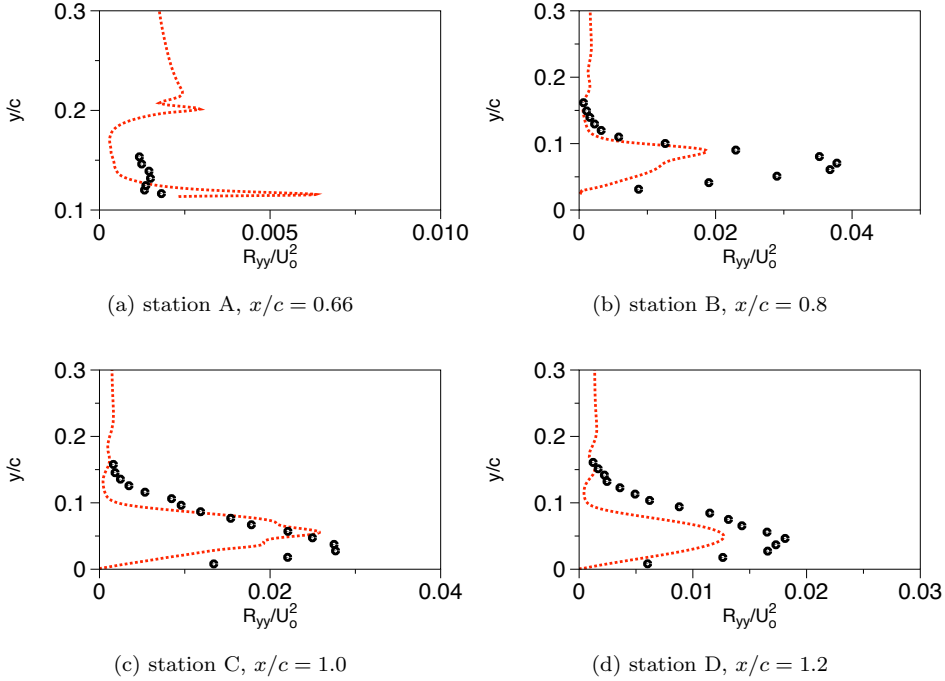


Figure 22: Turbulent flow over the “Glauert-Goldschmied” hill for the steady-suction case. Model predictions for the transverse Reynolds stress component R_{yy} at various x -stations for SA and ASBM-SA closures. Comparison is made to experimental values [18].

Results for the fluctuating shear stress component R_{xy} are shown in Figure 23. As shown, the hybrid ASBM-SA model is able to provide significantly improved predictions compared to the SA closure in the whole range of the recirculation region. Overall, ASBM-SA provides a satisfactory agreement with experiments.

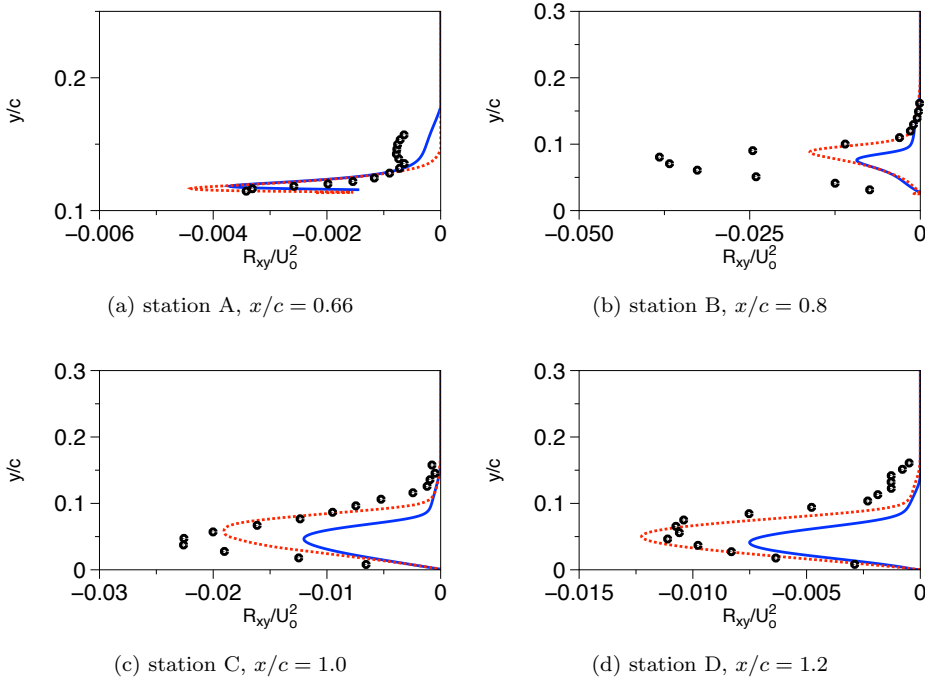


Figure 23: Turbulent flow over the “Glauert-Goldschmied” hill for the steady-suction case. Model predictions for the fluctuating shear stress component R_{xy} at various x -stations for SA and ASBM-SA closures. Comparison is made to experimental values [18].

The active control effect on the recirculation bubble is visualized in Figure 24. ASBM-SA model predictions for the streamlines of the mean velocity for both cases are shown, revealing a noticeable reduction of the bubble size.

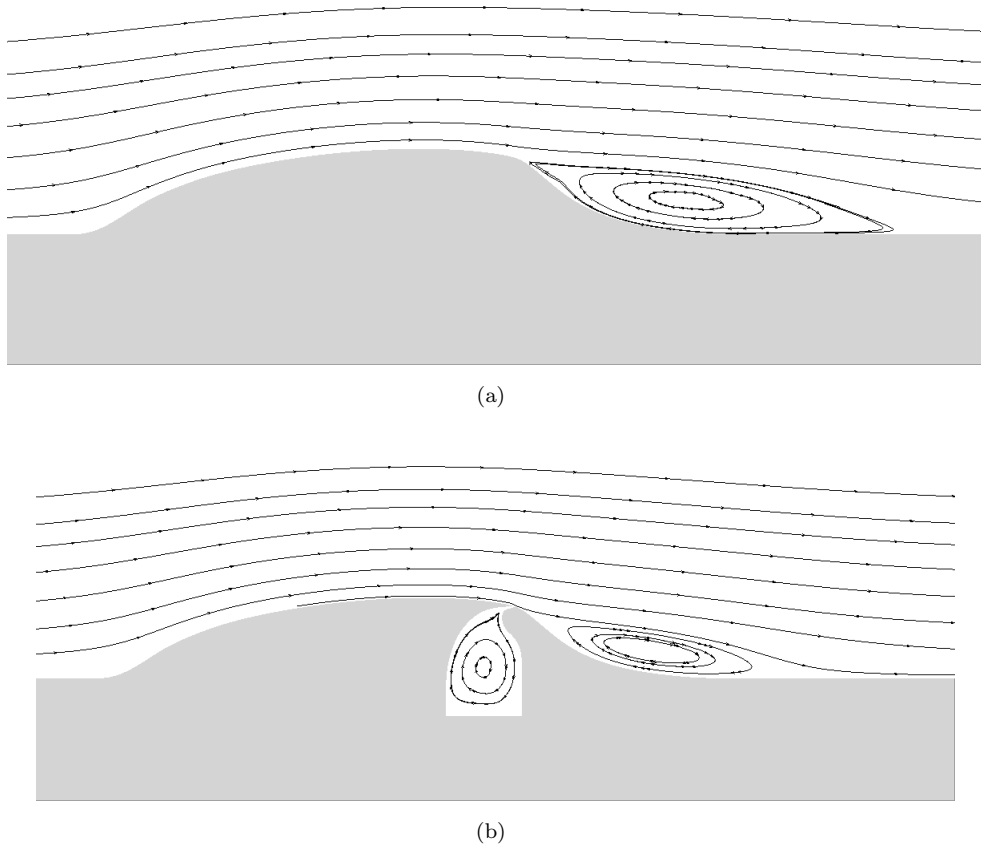


Figure 24: ASBM-SA model predictions for the streamlines of the mean velocity for (a) the uncontrolled case and (b) the controlled case .

4 Summary and Conclusions

The ASBM-SA closure has been tested for the case of a flow over a two-dimensional smooth hill in the shape of a “Modified Glauert-Goldschmied” hump both in the presence and absence of separation control. For both cases considered, the ASBM-SA model produced satisfactory predictions for the streamwise Reynolds stress component R_{xx} , while a qualitative agreement with the experiments was achieved for the transverse component R_{yy} . ASBM-SA closure provided improved predictions compared to SA for the shear stress at all stations. Regarding the mean quantities, the predictions of both closures are comparable, providing fair agreement with the experiments. Overall, the hybrid model managed to capture satisfactorily the traits of these highly anisotropic flows, while maintaining the high robustness of the SA model, at a good convergence rate. Use of separated zones for the activation of the filtering scheme resulted to smoother mean velocity profiles in the recirculation region, and more meaningful skin-friction profiles upstream and downstream the separated region.

As part of future work we intend to ascertain the performance of the hybrid model over challenging two-dimensional flows, such as turbulent flows around a wall-mounted cube and plane wall jets, while an extension

to three-dimensional smooth hills will be attempted. Regarding the refinement issues encountered in the current and previous works, further consideration is needed to understand why ASBM-SA delays further the re-attachment compared to SA for all validation cases considered until now, even though it gives better predictions for the shear stress over the entire region of the recirculation. We have already started developing more advanced filtering schemes, suitable for highly deformed meshes, since we believe that the choice of filtering scheme plays a role on the delay of flow's re-attachment, and contributes to yielding larger recirculation bubbles.

References

- [1] P. Spalart and S. Allmaras. A one-equation turbulence model for aerodynamic flows. *Recherche Aerospatiale*, 1:5–21, 1994. doi: 10.2514/6.1992-439.
- [2] S.C. Kassinos and W.C. Reynolds. A structure-based model for the rapid distortion of homogeneous turbulence. PhD Thesis, Thermosciences Division Department of Mechanical Engineering Stanford, California 94305, 1994.
- [3] S.C. Kassinos, W.C. Reynolds, and M.M. Rogers. One-point turbulence structure tensors. *J. Fluid Mech.*, 428:213–248, 2001. doi: 10.1017/S0022112000002615.
- [4] F.S. Stylianou, R. Pecnik, and S.C. Kassinos. A general framework for computing the turbulence structure tensors. *Comput. Fluids*, 106:54–66, 2015. doi: 10.1016/j.compfluid.2014.09.042.
- [5] C.F. Panagiotou and S.C. Kassinos. A structure-based model for the transport of passive scalars in homogeneous turbulent flows. *Int. J. Heat Fluid Fl.*, 57:109–129, 2016. doi: 10.1016/j.ijheatfluidflow.2015.11.008.
- [6] B. Shraiman and E. Sigg. Scalar turbulence. *Nature*, 405:639–646, 2000. doi: 10.1038/35015000.
- [7] S.C. Kassinos and W.C. Reynolds. A particle representation model for the deformation of homogeneous turbulence. pages 31–51. Annual Research Briefs, Center for Turbulence Research, 1996.
- [8] S.C. Kassinos and E. Akylas. *Advances in particle representation modeling of homogeneous turbulence. From the linear PRM version to the interacting viscoelastic IPRM*, volume 18. ERCOFTAC Series, 2012. doi: 10.1007/978-94-007-2506-5_6.
- [9] C.F. Panagiotou and S.C. Kassinos. A differential structure-based model based on stochastic evolution equations for the scalar turbulence parameters. European Conference on Computational Fluid Dynamics (ECFD 6), Barcelona, Spain, 2014.
- [10] S.V. Poroseva, S.C. Kassinos, C.A. Langer, and W.C. Reynolds. Structure-based turbulence model: Application to a rotating pipe flow. *Phys. Fluids*, 14(4):1523–1532, 2002. doi: 10.1063/1.1458008.
- [11] C.F. Panagiotou, F.S. Stylianou, and S.C. Kassinos. Structure-based transient models for scalar dissipation rate in homogeneous turbulence. *Int. J. Heat Fluid Fl.*, 82:108557, 2020.
- [12] C.F. Panagiotou and S.C. Kassinos. A structure-based model for transport in stably stratified homogeneous turbulent flows. *Int. J. Heat Fluid Fl.*, 65:309–322, 2017. doi: 10.1016/j.ijheatfluidflow.2016.12.005.
- [13] S.C. Kassinos, C.A. Langer, G. Kalitzin, and G. Iaccarino. A simplified structure-based model using standard turbulence scale equations: Computation of rotating wall-bounded flows. *Int. J. Heat Fluid Fl.*, 27:653–660, 2006. doi: 10.1016/j.ijheatfluidflow.2006.02.018.
- [14] C.A. Langer and W.C. Reynolds. A new algebraic structure-based turbulence model for rotating wall-bounded flows. PhD Thesis, Thermosciences Division Department of Mechanical Engineering Stanford, California 94305, 2003.
- [15] C.F. Panagiotou and S.C. Kassinos. The ASBM-SA turbulence closure: Taking advantage of structure-based modeling in current engineering CFD codes. *Int. J. Heat Fluid Fl.*, 52:111–128, 2015.
- [16] P. Bradshaw, D.H. Ferriss, and N.P. Atwell. Calculation of boundary layer development using the turbulent energy equation. *J. Fluid Mech.*, 28(3):593–616, 1967. doi: 0.1017/S0022112067002319.
- [17] C. Rumsey, T.B. Gatski, L. Sellers, V. Vatsa, and S. Viken. Summary of the 2004 CFD validation workshop on synthetic jets and turbulent separation control. In *AIAA 2004-2217*, 2004. doi: 10.2514/6.2004-2217.
- [18] D. Greenblatt, K.B. Paschal, N.W. Schaeffler, A.E. Washburn, J. Harris, and C. Yao. A separation control CFD validation test case. Part 1: Baseline and steady suction. In *2nd AIAA Flow Control Turbulence*, 2004. doi: 10.2514/6.2004-2220.
- [19] A. Seifert and L.G. Pack. Active flow separation control on wall-mounted hump at high Reynolds numbers. *AIAA J.*, 40(7):1363–1372, 2002. doi: 10.2514/2.1796.
- [20] T.B. Gatski and C. Rumsey. Langley Research Center Workshop: CFD validation of synthetic jets and turbulent separation control, (Cited 1 March 2020).